

This is the accepted manuscript made available via CHORUS. The article has been published as:

## Coupled evolution of composition and morphology in a faceted three-dimensional quantum dot

G. Vastola, V. B. Shenoy, J. Guo, and Y.-W. Zhang

Phys. Rev. B **84**, 035432 — Published 25 July 2011

DOI: [10.1103/PhysRevB.84.035432](https://doi.org/10.1103/PhysRevB.84.035432)

# Coupled evolution of composition and morphology in a faceted three-dimensional quantum dot

G. Vastola,<sup>1,\*</sup> V. B. Shenoy,<sup>2,†</sup> J. Guo,<sup>1</sup> and Y.-W. Zhang<sup>1</sup>

<sup>1</sup>*Institute of High Performance Computing, 1 Fusionopolis Way, #16-16 Connexis, Singapore 138632*

<sup>2</sup>*School of Engineering, Brown University, Providence, Rhode Island 02912, USA*

We study the coupled dynamical evolution of composition and morphology of a two-component alloy quantum dot in a faceted three-dimensional geometry. Using SiGe/Si as a model system, we perform simulations on the facet evolution and transition from a pyramidal to a domed shape, coupled with compositional evolution at different growth rates. We find that the composition profile in the quantum dot is growth history-dependent, and the growth rate can significantly influence the distribution of Ge atoms, indicating the importance of growth kinetics. In addition, we find that the aspect ratio of the quantum dot is affected by the composition distribution, highlighting the importance of the coupling between morphology and composition. Our present work may be useful in controlling the composition and morphology of quantum dots for applications in high-performance electronic devices.

PACS numbers: 81.10.Aj, 68.55.A-, 61.46.Hk, 61.66.Dk, 68.35.Md

During the growth of quantum dots in alloy semiconductor systems, such as SiGe/Si and InGaAs/GaAs, the coupled evolution of morphology and composition leads to a complex growth dynamics. As a consequence, the composition within the quantum dots may become highly non-uniform, and their shapes and sizes may change due to the coupling. It is well-known that the composition, shape and size of quantum dots greatly influence their electronic properties such as the band-gap alignment, the energy gap separation, and the position of confinement of electrons and holes<sup>1</sup>. Therefore, it is essential to develop an in-depth understanding of the growth dynamics of alloy quantum dots, which will aid in the fabrication of high performance quantum dot-based electronic devices, such as strained-gate field effect transistors<sup>2</sup>, new-generation lasers<sup>3</sup>, and spintronic devices<sup>4</sup>.

Tremendous efforts have been devoted to study the epitaxial growth of semiconductor quantum dots. In a previous paper<sup>5</sup>, a three-dimensional model was introduced to study the dynamical evolution of one-component nanostructures. This model was able to reproduce the formation of three-dimensional quantum dots over a substrate, and account for the processes of self-assembling and coarsening of quantum dots. A two-dimensional study was carried out to study the unfaceted growth of SiGe/Si heteroepitaxy<sup>6,7</sup>. These numerical simulations were able to describe the coupled evolution of morphology and composition during growth<sup>6</sup>. Alloying together with the three-dimensional faceted nature of a quantum dot was considered by minimizing the total energy of the crystal under the constraint of a constant average composition. This work predicted a composition distribution that was in qualitative agreement with experiments<sup>8,9</sup>, and was recently extended to include the presence of dislocations<sup>10,11</sup>.

To our knowledge, none of those previous studies have simultaneously considered all the following features, important to the growth of alloying quantum dots: three-dimensional geometry, composition segregation, surface

facets and dynamical evolution. Recently, the equations that govern the evolution of composition and morphology, and account for the *faceted* nature of a crystal, have been derived from first-principles thermodynamics<sup>12</sup> (for comparison with the case of unfaceted surfaces, see for example<sup>7,13,14</sup>). These equations provide a theoretical framework to simulate the growth dynamics of alloy quantum dots. In the present work, we employ this framework to study the coupled evolution of shape, size and composition of a faceted three-dimensional quantum dot upon growth. We focus on the morphological evolution and compositional patterning of the quantum dots.

## I. MODEL FORMULATION

The governing equations for the growth of a three-dimensional fully-faceted crystal have been recently derived from first-principles thermodynamics<sup>12</sup>; here, we formulate these equations for the case of a quantum dot and implement them in our numerical calculations.

Consider a three-dimensional alloy crystal made of two elements A and B, as schematically represented in Fig. 1(a), immersed in a mixed vapor phase of A and B, and let  $\zeta$  be the composition of B in the AB alloy. In general, A and B are completely specified by the value of their lattice parameters, stable crystallographic facets, and surface energies of their respective pure crystals. Growth is modeled in the Surface Attachment Limited Kinetics (SALK) regime, where material is exchanged between the solid and the vapor through attachment-detachment kinetics. The choice of this limiting regime, as opposed to the Diffusion Limited (DL) kinetics regime, is motivated by the fact that crystalline growth from vapour phase requires high temperatures (600-700° C). At these temperatures, growth should not be limited by surface diffusion.

In the SALK regime, surface evolution is governed by the difference in chemical potential between the solid and

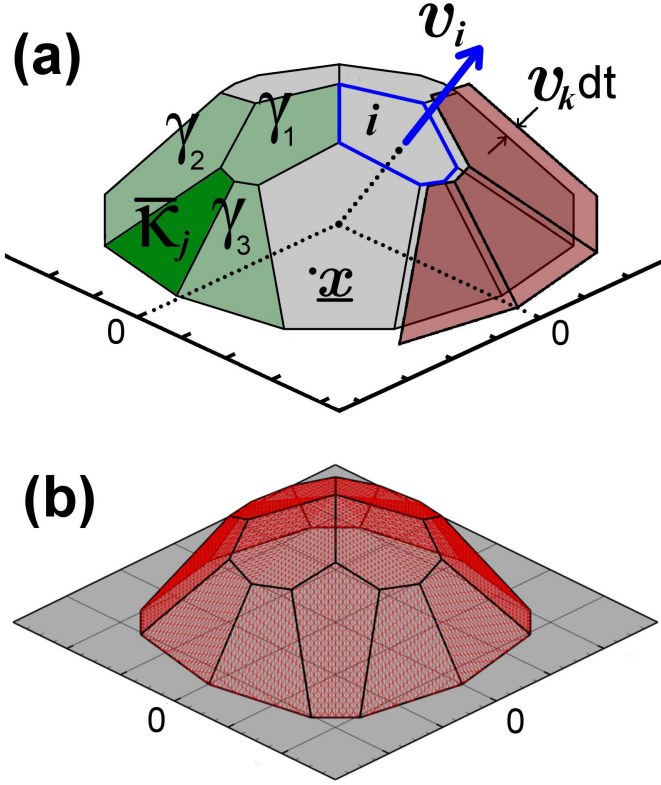


FIG. 1. (color online) (a) Illustration of a typical dot shape (dome island in Ge/Si heteroepitaxy) showing how the change of one facet surface energy,  $\bar{\kappa}_j$ , relates to the surface energies of that facet and its surrounding ones. When a facet shares an edge with the substrate, the surface energy of the substrate needs to be considered, to calculate the weighted mean curvature  $\bar{\kappa}_j$  of facet  $j$ , which also depends on the surface energies of the neighboring facets  $\gamma_1, \gamma_2$ , and  $\gamma_3$ . For each facet, the normal velocity  $v_i$  (positive or negative) is calculated at each time step, and the position of all the facets in the three-dimensional crystal shape is then updated (light red). (b) Three-dimensional grid used in the numerical calculation. Crystal shape is reconstructed using a set of points evolving with time. The grid has a regular spacing across the surface, except for the points at the edges and at the boundary, which track the facets and the boundary between the crystal and the substrate, respectively.

the vapor phase. If the crystal is fully faceted during evolution, the chemical potentials for A and B at the crystal's surfaces are<sup>12</sup>

$$\begin{aligned}\mu_{Ai}(\mathbf{x}, t) &= \alpha_i(\mathbf{x}, t) - \zeta(\mathbf{x}, t)\beta_i(\mathbf{x}, t) \\ \mu_{Bi}(\mathbf{x}, t) &= \alpha_i(\mathbf{x}, t) + (1 - \zeta(\mathbf{x}, t))\beta_i(\mathbf{x}, t),\end{aligned}\quad (1)$$

with

$$\alpha_i(\mathbf{x}, t) = U_b + \frac{1}{2}\sigma_{ij}\varepsilon_{ij} + \bar{\kappa}_i,$$

$$\beta_i(\mathbf{x}, t) = \frac{1}{\delta} \frac{\partial \gamma_i}{\partial \zeta} + \varepsilon_0 \sigma_{kk}. \quad (2)$$

where  $U_b$  is the internal energy, which includes the binding energy and the entropy<sup>15</sup>,  $\sigma_{ij}$  and  $\varepsilon_{ij}$  are the stress and strain tensors, respectively, and  $\bar{\kappa}_i$  is the weighted mean curvature of facet  $i$ . The last term quantifies the change in the total surface energy corresponding to a small movement of facet  $i$  in the direction pointing outwards the crystal surface. For the case of a quantum dot, we consider

$$\bar{\kappa}_i = \frac{1}{S_i} \sum_{j \neq i} \frac{(\delta_j \gamma_{Bj} - c_{ij} \gamma_{Bi}) l_{ij}}{\sqrt{1 - c_{ij}^2}}, \quad (3)$$

where the sum is over all the facets neighboring to facet  $i$ ,  $\gamma_{Bj}$  is the surface energy density of facet  $j$ ,  $S_i$  is the surface area exposed by facet  $i$ ,  $l_{ij}$  is the length of the edge shared between facets  $i$  and  $j$ , and  $c_{ij} = \mathbf{n}_i \cdot \mathbf{n}_j$  is the scalar product between the unit normals of facets  $i$  and  $j$ , respectively. The parameter  $\delta_j$  accounts for the fact that, for the facets sharing an edge with the substrate, the interface energy between the crystal and substrate needs to be considered. Therefore,  $\delta_j$  equals  $+1$  if  $j$  is a regular facet, and  $-1$  if  $j$  is the substrate. The form (3) accounts for the surface segregation effect by assuming the surfaces pure in the component B. This assumption is justified by the fact that the time scale for local atom exchange between the surface and the region immediately below is much faster than that for the deposition from the vapor phase. The expression (3) is consistent with the form derived by Carter *et al.*<sup>13</sup> for the case of one-component fully faceted crystals.

Following the attachment (or detachment) of atoms at the surfaces, the facets move with a given velocity. Evolution consistent with the decrease of Gibbs free energy requires that the individual-component facet velocities take the form<sup>12</sup>

$$\begin{aligned}v_{Ai}(\mathbf{x}, t) &= M_A (\mu_A^0 - \bar{\mu}_{Ai}) + \frac{1}{4} (M_A + M_B) (\beta_i(\mathbf{x}, t) - \bar{\beta}_i) \\ v_{Bi}(\mathbf{x}, t) &= M_B (\mu_B^0 - \bar{\mu}_{Bi}) - \frac{1}{4} (M_A + M_B) (\beta_i(\mathbf{x}, t) - \bar{\beta}_i)\end{aligned}$$

where  $\bar{\mu}_{Ai}$  and  $\bar{\mu}_{Bi}$  are the averages of  $\mu_{Ai}$  and  $\mu_{Bi}$  over facet  $i$ , respectively. The above form of the velocities ensure that the sum of  $v_{Ai}(\mathbf{x}, t)$  and  $v_{Bi}(\mathbf{x}, t)$ , which is the velocity of facet  $i$ , is rigorously constant across the facet, ensuring that the facet does not “break up”<sup>12</sup>. The parameters  $M_A$  and  $M_B$  are the attachment rates of species A and B, respectively. Although the attachment rates may be different on each facet<sup>12</sup>, here, for simplicity, we assume them to be independent of crystalline orientation.

We now consider the vapor phase surrounding the crystal. Under the SALK regime, material incorporates at a constant rate (volume per unit time)  $R_A$  and  $R_B$  for each species independently. The composition of the depositing material, therefore, is  $\frac{R_B}{R_A + R_B}$ . For attachment rates independent of facet orientation, the chemical potentials

for A and B are obtained from the general expression<sup>12</sup> as

$$\begin{aligned}\mu_A^0 &= \frac{1}{S_{TOT}} \left( \sum_{i=1}^N S_i \bar{\mu}_{Ai} + \frac{R_A}{M_A} \right) \\ \mu_B^0 &= \frac{1}{S_{TOT}} \left( \sum_{i=1}^N S_i \bar{\mu}_{Bi} + \frac{R_B}{M_B} \right),\end{aligned}\quad (5)$$

where  $S_{TOT}$  is the total surface area exposed by the crystal.

To model the evolution of composition with time, we assume that material intermixing only occurs within a thin surface layer of thickness  $\delta^7$  that rigidly follows the geometrical surfaces of the crystal. If the surface is advancing, the composition evolves as

$$\delta \frac{\partial \zeta}{\partial t} = v_{Bi}(\mathbf{x}, t) - \zeta(\mathbf{x}, t) v_i(t) \quad (6)$$

while  $\zeta$  assumes the value of the bulk if the surface is receding. Here,  $v_i(t) = v_A(\mathbf{x}, t) + v_B(\mathbf{x}, t)$  is the total velocity of facet  $i$ .

The set of Eqs. 1-6 represent the governing equations that are used in the present work. Our aim is to develop a numerical scheme, which is able to solve this set of coupled equations, and to illustrate the crystal growth dynamics. The numerical scheme is described in the following Section.

## II. NUMERICAL SCHEME

SALK dynamics was implemented in the following steps. A discrete grid of points was introduced to track the crystal surface at all times. To accurately describe the evolution of shape and composition, and track the position and evolution of facets' edges with time, the grid was refined in correspondence to the crystal's edges, and to the boundary of the crystal with the substrate. A typical realization of the grid is shown in Fig. 1(b). A learn-on-the-fly algorithm was implemented to keep track of the changes in shape (moves of the edges), and to account for the possibility that, during the shape evolution, a new facet may be nucleated at a point on the grid. Variables specifying stress, strain, surface energy, chemical potential and composition were assigned at each grid point.

In our scheme, dynamics is completely described with  $N+5$  parameters, where  $N$  is the number of all the possible stable facets of the A-B system (note that the number of facets present on the crystal at time  $t$  may be a subset of  $N$ , see Sec. IIA). These are  $N$  values of the surface energy densities  $\gamma_{Bi}$ ,  $i = 1, \dots, N$  of facets of pure B. Then, another two parameters are the attachment rates  $M_A$  and  $M_B$  for A and B, respectively. Another parameter is the lattice mismatch between A and B; finally, the

last two parameters are deposition rates  $R_A$  and  $R_B$  for each species.

Crystal growth was simulated in the following way. The starting point is represented by an arbitrary choice of crystal shape and composition. At each loop of computation, the possibility that a facet can nucleate or disappear (if its size is small enough) is evaluated; the criterion used to determine the nucleation of a new facet is discussed in Sec. IIA. After the shape is established, strain and stress tensors are computed at each point of the grid using the method described in Sec. IIB. The chemical potentials of the two atomic species are computed for both the solid and its surrounding vapor phase following Eq. 1 and Eq. 5. Then, the velocity of each facet is evaluated using Eq. 4. Once the velocities are known at time  $t$ , the positions of the facets at time  $t + dt$  are derived by integrating the velocities over time. Starting from the position of the crystallographic planes at time  $t + dt$ , in turn, the three-dimensional crystal shape is calculated as the convex hull of the planes at time  $t + dt$ . The variations of composition during the time step are calculated using Eq. 6. The code performing the set of operations described above was written in-house using C language.

### A. Nucleation and disappearance of facets

During growth, new facets may nucleate, or small facets may disappear due to the variations in surface chemical potential. We will first consider the case of facet nucleation, and then describe the case of facet disappearance.

If surface motion is governed only by surface energy, nucleation of a new facet follows a *local* criterion, associated only with the facet under consideration<sup>13</sup>. In this case, if a small facet with zero chemical potential is added onto the crystal without changing the total chemical potential, the incorporation is allowed. For the case of a crystal under strain, however, a local criterion is insufficient. In this case, the presence of a new facet at a given position can alter the total energy of the crystal. Therefore, a *global* criterion has to be established. A new facet can be added in the crystal if the change in total energy arising from the addition of the new facet,

$$\sum_{i=1}^{N+1} \int_{S_i} [((1 - \zeta) \mu_{Ai} + \zeta \mu_{Bi})] dS_i, \quad (7)$$

is lower than that of the crystal without the new facet,

$$\sum_{i=1}^N \int_{S_i} [((1 - \zeta) \mu_{Ai} + \zeta \mu_{Bi})] dS_i, \quad (8)$$

where the comparison is made between crystals of the same volume.

The nucleation of new facets was implemented in the following way. At a constant interval (for example, every

100 time steps), a shape containing a small new facet in an otherwise identical crystal shape was produced. Then, the nucleation criterion established by Eq. 7 - 8 was evaluated. If the nucleation of a new facet is allowed, the facet is then incorporated into the crystal.

When a facet advances faster than the neighboring ones, its corresponding size decreases because the shape of the crystal is convex. Ultimately, this facet may shrink to zero size, and is simply removed from the crystal shape. Therefore, the treatment of facet disappearance is straightforward, and does not require any criterion based on the evaluation of chemical potentials.

### B. Calculation of surface strain and stress

Evaluation of the chemical potentials, Eq. 1, requires detailed knowledge of the stress and strain tensors at the surface. This calculation is performed using the method of Xiang et al.<sup>16</sup>, and proceeds in the following manner. The three-dimensional surface profile is first decomposed in its Fourier components. Then, the stress and strain tensors are evaluated for each component. Finally, inverse Fourier transform is performed to obtain the stress and strain tensors at each point on the surface. For this task, the same grid of points introduced earlier in this Section (see Fig. 1) is used. Here, it is worth mentioning that for an  $N \times N$  grid, the computational cost of the calculation scales with  $N^2$ , and therefore a balance between accuracy and performance has to be sought.

## III. RESULTS AND DISCUSSION

The numerical scheme proposed in the preceding Section is general and, in principle, can be applied to any two-component system. Here, we use the SiGe/Si as a model system to show the predictive capability of the method. The reason that we use this model system is because the measurements of the composition profiles, as well as the shape of the nanocrystals, have been recently performed<sup>17-19</sup>. Therefore, let us begin by setting  $A = \text{Si}$ ,  $B = \text{Ge}$ .

A small pyramid with base size 5nm and  $\{105\}$  facets was chosen the initial state. The Ge composition was set uniform initially, at a value of 0.5. Two other facets, namely the  $\{113\}$  and the  $\{15\ 3\ 23\}$ , which are both known to be stable facets for Ge<sup>20,21</sup> were also included. To account for the surface segregation effect (see Sec. I), the composition of the surfaces was assumed to be 100% Ge, and therefore the values of surface energies used were the ones for pure Ge. From the detailed *ab initio* calculations carried out for these facets<sup>20-22</sup>, and recent insights gained on the stability of the  $\{15\ 3\ 23\}$  facet<sup>23</sup>, the following values of surface energy were used:  $\gamma_{105} = 61.5 \text{ meV/\AA}^2$ ,  $\gamma_{113} = 62 \text{ meV/\AA}^2$ , and  $\gamma_{15323} = 68 \text{ meV/\AA}^2$ . The choice made for the surface energy of the  $\{105\}$  facet reflects the stabilization effect due to compressive

strain<sup>22,24</sup>. Following Haynes *et al.*<sup>25</sup>, the ratio of attachment rates between Ge and Si was set to  $M_{\text{Ge}}/M_{\text{Si}} = 10^4$ . While this value was extracted for the case of Solid Phase Epitaxy (SPE) growth of SiGe alloy, we assume that a similar value holds for the case of crystallization from vapor phase.

Representative snapshots of the resulting dynamics are shown in Fig. 2. Starting from the initial state, (see the arrow in Fig. 2(a)), the initial incorporation of material produces a very fast growth, because material is attaching on a very small island at constant rate. As volume increases, nucleation of  $\{113\}$  and  $\{15\ 3\ 23\}$  then follows in an absolutely natural fashion. The precise time and volume at which they are inserted are given exclusively by the criterion established in Sec. II A. Insertion of new facets is thermodynamically favored because they are more effective in relieving strain than the shallow  $\{105\}$  facets.

Snapshots (c-e) in Fig. 2 represent the shape evolution and transition from the pyramid to the dome, a typical process observed in the Ge/Si system<sup>26</sup>. In the present work, the introduction of facets was observed first for  $\{113\}$  facets (see 2 (c)), and then followed by  $\{15\ 3\ 23\}$  facets (see 2 (d)). The shape transition from pyramids to domes were reported by Ross et al.<sup>27</sup> using Scanning Tunneling Microscopy (STM). They showed the initial incorporation of  $\{113\}$  facets and then also followed by  $\{15\ 3\ 23\}$  facets. Our calculation results are consistent with their experimental observations.

After each of the steep facets are incorporated and the dome shape is established, dynamics proceeds as shown in panels (f)-(h) of Fig. 2. In particular, it is possible to appreciate the coupling between the evolution of shape and composition: The shallow facets, progressively, reduce their size at the gain of the steep ones, which grow. Simultaneously, segregation of the species with the larger lattice parameter (Ge) occurs at the top of the islands and along the edges. At the same time, the species with the smaller lattice parameter (Si) locates at the lower corners and base of the island. This redistribution allows for a lowering of the elastic energy of the crystal, and is consistent with the results shown in other works<sup>8,9,11</sup>.

With further growth, it comes natural to ask what is the ultimate shape of the crystal. With increasing volume, nucleation of defects will eventually represent the optimal way to release elastic energy. If the nucleation of defects is suppressed, our calculations indicate that the final shape of the evolution is a pure  $\{15\ 3\ 23\}$  pyramid (not shown) with both the  $\{105\}$  and the  $\{113\}$  facets completely disappeared. However, such steep pyramid has never been observed experimentally, indicating that the critical volume for defect incorporation is smaller than that for the formation of the steep  $\{15\ 3\ 23\}$  pyramid.

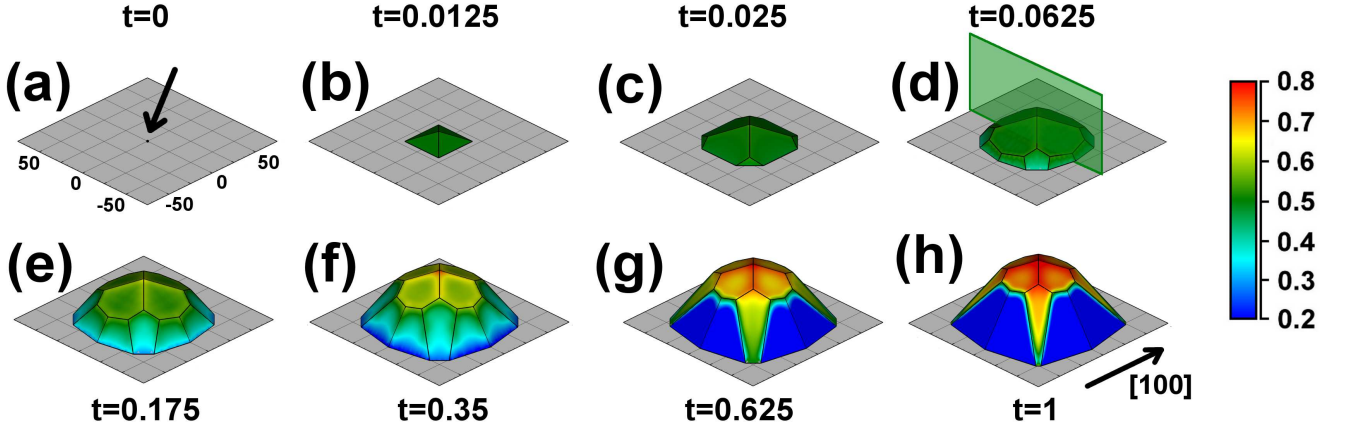


FIG. 2. (color online) Crystal growth predicted for the SiGe/Si system. Starting from the initial state, represented by a small  $\{105\}$  pyramid of 0.5 uniform Ge composition (a) and with increasing time  $t$ , the shape grows (b) and subsequently incorporates the set of  $\{113\}$  (c) and  $\{15\ 3\ 23\}$  (d) facets. Evolution continues with a progressive reduction in size of shallow facets in favor of the steep ones (e), coupled with segregation of Ge at the island top, and of Si at the island base (f-g). Evolution proceeds towards the typical shape of a dome of GeSi heteroepitaxy (g), ultimately showing a strong composition segregation and the shrinkage of  $\{113\}$  facets. Color scale represents the composition of Ge atoms. In (d), the vertical plane shows the location of the cross section used to calculate Ge composition profile. Notice that the plane is fixed, while the crystal is growing. Lengths are in nm.

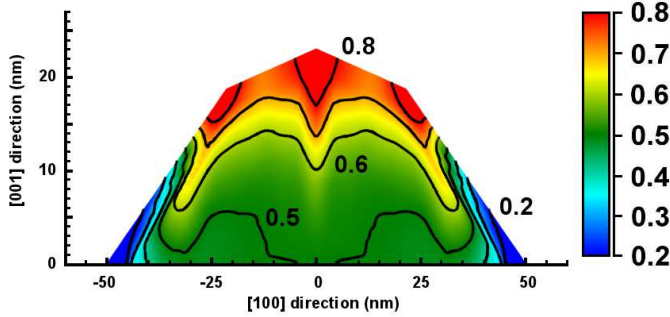


FIG. 3. (color online) Cross-sectional composition profile extracted from the evolution of Fig. 2, along the direction shown in Fig. 2(d). Segregation of Ge occurs at the top of the island, while Si is located at the bottom region. Clearly the composition profile shows the growth history-dependent: the inner parts of the composition profile represent the initial stages of growth, while the near surface region represents the later stages of growth. Therefore, a cross-sectional profile indeed traces the *history* of evolution of the crystal.

#### A. Cross-sectional composition profiles

The cross-sectional composition profile taken along the  $[100]$  direction and corresponding to Fig. 2(h) is shown in Fig. 3. The segregation of Ge at the top of the island, as well as of Si at the corners and base, is evident.

At this stage, it is worth comparing the profile obtained here with experimental results. It has been demonstrated that reciprocal space mapping method from X-ray diffraction<sup>17,19</sup> and composition-selective chemical etching<sup>18</sup> are both techniques capable of reconstructing composition profiles in cross-section. The measure-

ments<sup>17-19</sup> showed that Ge atoms accumulate at the top of the island and silicon atoms prefer to stay at the bottom. The composition at the central part of the island appears to be relatively uniform with a composition close to the average between the top and bottom of the islands. Overall, their composition profiles are in qualitative agreement with that obtained here as shown in Fig. 3.

Besides the comparison with experimental measurements, our dynamic approach allows for a different interpretation of the composition profiles. During the growth, the crystal evolves in both composition and morphology. Therefore, the composition map in cross-sections reveals the growth *history* of the crystal, from the past (the inner bulk) to the present (the surfaces).

#### B. Effect of growth rate on composition distribution

We study the effect of the growth rate on the composition and shape evolution of the crystal by keeping all the other parameters (specifically, the surface energies, attachment rates and initial conditions) unchanged. In the previous case, the growth rate was taken as  $R_{\text{Ge}} = R_{\text{Si}} = R_{\text{ref}} = 10.0 \cdot 10^2 \text{ nm}^3/\text{sec}$ . Here two more growth rates are used: one is  $R_{\text{low}} = 7.5 \cdot 10^2 \text{ nm}^3/\text{sec}$ , which is lower than the previous one, and the other is  $R_{\text{high}} = 20 \cdot 10^2 \text{ nm}^3/\text{sec}$ , which is higher. These values were chosen such that, considering the size of the simulation cell of  $150 \times 150 \text{ nm}$ , they give rise to a linear growth rate of the order of  $1 \text{ \AA}/\text{sec}$ , which is a typical value in experiments. For each evolution, the cross-sectional composition profile along the  $(100)$  cut was extracted,



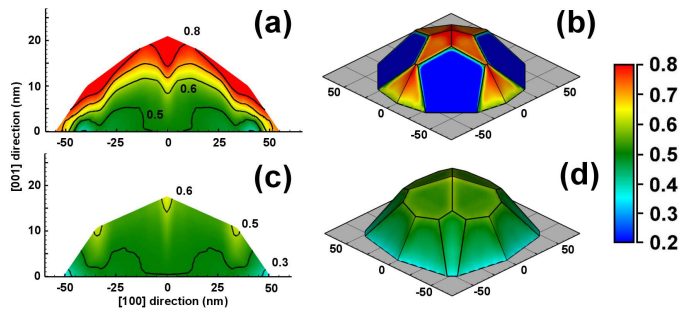


FIG. 4. (color online) Vertical cross sectional composition distribution as a result of different growth rates, namely  $R_1$  (a) and  $R_2$  (c). For each profile, the corresponding shape and surface composition are shown in panels (b) and (d), respectively. By comparing the panels, the effect of growth rate is evident: composition distribution becomes more uniform at higher growth rates. Due to the coupling among shape, strain and composition, the final shape is also affected by the growth rate: panels (b) and (d) show that the size of the  $\{15\ 3\ 23\}$  facets is smaller at a lower growth rate, while is larger at a higher growth rate (d).

and the comparison is shown in Fig. 4.

Careful comparison of the composition profile in panels (a) and (c) in Fig. 4, and the profile in Fig. 3, shows that the effect of increasing growth rate is primarily to increase the uniformity of composition distribution: The amount of segregation in panel (c), where the growth rate is higher, is clearly much lower than that in panel (a), where growth is slower. Obviously, at very high growth rates, the minor segregation occurs only at the corners, leaving behind “trails” of segregated material into the bulk, as shown in panel (c) of Fig. 4.

The increase in composition uniformity at high growth rates can be understood in terms of the time scales involved in the growth dynamics. At high growth rates, material does not have the time to segregate because the surface layer is quickly covered by new materials and become part of bulk. As a result, the overall composition redistribution is quite uniform. On the other hand, at low growth rates material is allowed to have sufficient time to redistribute across the surface, and therefore segregation dominates. In fact, the composition profile at low growth rates as shown in Fig. 4 (a) is very similar to that obtained by minimizing the elastic energy<sup>8,9,11</sup>, indicating that the growth at a lower deposition rate is a process closer to the thermodynamic equilibrium.

Due to the coupling to the evolution of composition, crystal shape is also affected by the growth rate. Fig. 4(b) and (d) depict the three-dimensional shape and composition corresponding to the growth at  $R_{low}$  and  $R_{high}$  given above. It is seen that at the low growth rate, the surface area exposed by the steep facets  $\{15\ 3\ 23\}$  is smaller than that at the high growth rate. This finding can be explained on the following basis: At a low growth rate, as we have seen, material mixing is more pronounced. Therefore, there is less need to incorpo-

rate steep facets, which represent an alternative route towards the relaxation of elastic energy. On the other hand, when the growth rate is high and material redistribution is quenched, the only remaining path allowed for strain energy relaxation is the incorporation and growth of steep facets, as shown in Fig. 4(d).

As evident from panel (b) of Fig. 4 and panel (g) of Fig. 2, facets of different sizes have an average composition significantly different from each other. For example, the largest facets  $\{113\}$  in Fig. 4 (b) are the ones richest in Si, and the largest facets  $\{15\ 3\ 23\}$  in (Fig. 2(g)) are also richest in Si. We interpret this feature as a consequence of the coupled evolution among shape, size and composition during growth. When the facet area is large, the presence of Ge atoms is not favorable to relax the strain energy due to its atomic size. Therefore, a large facet tries to remove Ge atoms and put them either on the island top or at the facet edges. Indeed, recent experimental work<sup>28</sup> based on X-ray analysis of the three-dimensional composition profile has shown that different facets have an average composition unambiguously different from each other.

Our calculation results clearly show a high growth rate leads to the uniform composition profile within the island. Therefore, the assumption of a uniform material distribution at sufficiently high growth rate is valid<sup>29</sup>.

### C. Effect of growth rate on aspect ratio

Given a three-dimensional convex crystal on a substrate surface, define its aspect ratio  $\alpha$  as

$$\alpha = \frac{h}{\sqrt{S_b}} \quad (9)$$

where  $h$  is the crystal height and  $S_b$  is its island base area. By computing  $\alpha$  with respect to time, we obtain the plot shown in Fig. 5. In this figure, the aspect ratios corresponding to the growth rates at  $R_{low}$ , and  $R_{high}$  are shown as a function of the crystal volume, i.e. the product  $Rt$ . Since the growth rates are different, it is necessary to use volume as the variable rather than time.

Figure 5 shows the evolution of aspect ratio from the value of 0.1, typical of the  $\{105\}$  pyramid, to values around 0.2, typical of the dome-shaped islands. Two main features can be identified: the first for the early stage of the evolution, and the second at the later stage of growth.

Comparing the curve for a low (red curve) and that for a high (blue curve in Fig. 5) growth rate, the critical volume for the nucleation of steep facets is smaller at a higher growth rate (see the inset in Fig. 5). This finding is consistent with the comments made previously in Sec. III B, where differences in crystal shape were related to different growth rates. Two paths are available for elastic-energy release: segregation, and/or incorporation of steep facets. At a low growth rate, when segregation

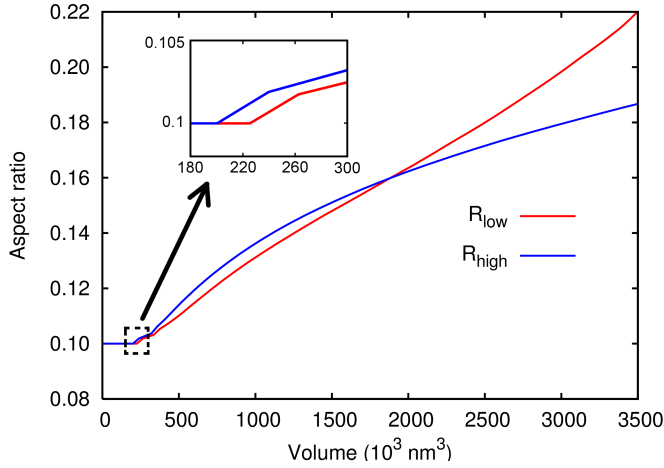


FIG. 5. (color online) Evolution of island aspect ratio as a function of the volume of material deposited, for two values of growth rate :  $R_{low}$  (red solid line), and  $R_{high}$  (blue solid line). With increasing time, the aspect ratio increases from 0.1 (the value of  $\{105\}$  pyramid) to  $\approx 0.2$ , i.e. the typical value of a dome-shaped island. An increase in aspect ratio occurs at a smaller critical volume at a high growth rate, because the incorporation of steep facets is the only possible path to relieve elastic energy, as opposed to segregation, which is the dominant mechanism at a low growth rate. Because segregation lowers the elastic energy of the system at a lower growth rates, the incorporation of steep facets is retarded, compared to the evolution at a higher growth rate (see the inset). At large island volumes, the increase in aspect ratio is more pronounced at a low growth rate because segregation is increasing the velocity of the top facets, and therefore, the resulting shape has a high aspect ratio.

is the dominant mechanism, the need for incorporation of steep facets is less severe. Therefore, the aspect ratio starts to increase at a larger volume compared to that at a high growth rate, where segregation is quenched and therefore incorporation of steep facets is the only path available to relieve elastic energy (Fig. 5).

At the later stages of growth (Fig. 5, right), it is seen that an island reaching the highest aspect ratio is the one grown at the lowest growth rate, and vice versa. Obviously, the aspect ratio may increase for two reasons: increase in the island height, or decrease in the island base. At a low growth rate where segregation is dominant, the velocity of the  $\{105\}$  facets is high due to the high Ge composition. Therefore, the increase in aspect ratio is sharp compared to the growth at a high growth rate, where the quenched segregation results in a lower velocity of the  $\{105\}$  facets.

#### IV. CONCLUSIONS

In conclusion, we have developed a numerical method to study the growth of fully faceted three-dimensional crystals in the surface attachment limited kinetics

regime. Using SiGe/Si as a model system, we have studied the influence of growth rate on composition evolution, and shown that a high growth rate promotes the uniformity of the alloy inside the crystal, while a low growth rate results in a significantly non-uniform alloy redistribution. We have also investigated the coupling between shape and composition evolution, and shown the important role of growth rate in dictating the island shape. This understanding might be useful in controlling the morphology and composition of quantum dots for applications in high-performance devices.

#### ACKNOWLEDGMENTS

The financial support provided by the Visiting Investigatorship Programme “Size Effects in Small Scale Materials” as well as by NSF Grants CMMI-0825771, DMS-0854919, and DMS-0914648 and DOE contract DE-FG02-01ER45913 is gratefully acknowledged.



- 
- \* vastolag@ihpc.a-star.edu.sg  
† Vivek.Shenoy@brown.edu
- <sup>1</sup> M. Brehm, T. Suzuki, T. Fromherz, Z. Zhong, N. Hrauda, F. Hackl, J. Stangl, F. Schäffler, and G. Bauer, *New J. Phys.* **11**, 063021 (2009).
  - <sup>2</sup> V. Jovanovic, C. Biasotto, L. K. Nanver, J. Moers, D. Grutzmacher, J. Gerharz, G. Mussler, J. van der Cingel, J. J. Zhang, G. Bauer, O. G. Schmidt, and L. Miglio, *IEEE Electron Device Letters* **31**, 1083 (2010).
  - <sup>3</sup> P. Rauter, T. Fromherz, N. Q. Vinh, B. N. Murdin, G. Mussler, D. Grützmacher, and G. Bauer, *Phys. Rev. Lett.* **102**, 147401 (2009).
  - <sup>4</sup> A. A. Khajetoorians, B. Chilian, J. Wiebe, S. Schuwalow, F. Lechermann, and R. Wiesendanger, *Nature* **467**, 1084 (2010).
  - <sup>5</sup> Y.-W. Zhang, *Phys. Rev. B* **61**, 10388 (2000).
  - <sup>6</sup> Y. Tu and J. Tersoff, *Phys. Rev. Lett.* **98**, 096103 (2007).
  - <sup>7</sup> B. J. Spencer, P. W. Voorhees, and J. Tersoff, *Phys. Rev. B* **64**, 235318 (2001).
  - <sup>8</sup> N. V. Medhekar, V. Hagadekatte, and V. B. Shenoy, *Phys. Rev. Lett.* **100**, 106014 (2008).
  - <sup>9</sup> R. Gatti, F. Uhlík, and F. Montalenti, *New J. Phys.* **10**, 083039 (2008).
  - <sup>10</sup> N. V. Medhekar, V. Hegadekatte, and V. B. Shenoy, *Solid State Comm.* **149**, 1395 (2009).
  - <sup>11</sup> H. Ye, P. F. Lu, Z. Y. Yu, D. L. Wang, Z. H. Chen, Y. M. Liu, and S. M. Wang, *Sol. State Comm.* **150**, 1275 (2010).
  - <sup>12</sup> V. B. Shenoy, *J. Mech. Phys. Sol.* **59**, 1121 (2011).
  - <sup>13</sup> W. C. Carter, A. R. Roosen, J. W. Cahn, and J. E. Taylor, *Acta Metall. Mater.* **43**, 4309 (1995).
  - <sup>14</sup> J. Tersoff, *Appl. Phys. Lett.* **83**, 353 (2003).
  - <sup>15</sup> J. Y. Tsao, *Materials Fundamentals of Molecular Beam Epitaxy*, ninth ed. (Academic Press, San Diego, CA, 1993).
  - <sup>16</sup> Y. Xiang and W. E. J. Appl. Phys. **91**, 9414 (2002).
  - <sup>17</sup> G. Medeiros-Ribeiro and R. S. Williams, *Nano Lett.* **7**, 223 (2007).
  - <sup>18</sup> A. Rastelli, M. Stoffel, A. Malachias, T. Merdzhanova, G. Katsaros, K. Kern, T. Metzger, and O. G. Schmidt, *Nano Lett.* **8**, 1404 (2008).
  - <sup>19</sup> T. Schüllli, G. Vastola, M. Richard, A. Malachias, G. Renaud, F. Uhlík, F. Montalenti, G. Chen, L. Miglio, F. Schäffler, and G. Bauer, *Phys. Rev. Lett.* **102**, 025502 (2009).
  - <sup>20</sup> A. Stekolnikov and F. Bechstedt, *Phys. Rev. B* **72**, 125326 (2005).
  - <sup>21</sup> Z. Gai, X. Li, R. G. Zhao, and W. S. Yang, *Phys. Rev. B* **57**, R15060 (1998).
  - <sup>22</sup> D. B. Migas, S. Cereda, F. Montalenti, and L. Miglio, *Surf. Sci.* **556**, 121 (2004).
  - <sup>23</sup> M. Brehm, F. Montalenti, M. Grydlik, G. Vastola, H. Lichtenberger, N. Hrauda, M. J. Beck, T. Fromherz, F. Schäffler, L. Miglio, and G. Bauer, *Phys. Rev. B* **80**, 205321 (2009).
  - <sup>24</sup> V. B. Shenoy, C. V. Ciobanu, and L. B. Freund, *Appl. Phys. Lett.* **81**, 364 (2002).
  - <sup>25</sup> T. E. Haynes, M. J. Antonell, C. A. Lee, and K. S. Jones, *Phys. Rev. B* **51**, 7762 (1995).
  - <sup>26</sup> F. Montalenti, P. Raiteri, D. B. Migas, H. von Känel, A. Rastelli, C. Manzano, G. Costantini, U. Denker, O. G. Schmidt, K. Kern, and L. Miglio, *Phys. Rev. Lett.* **93**, 216102 (2004).
  - <sup>27</sup> F. M. Ross, R. M. Tromp, and M. C. Reuter, *Science* **286**, 1931 (1999).
  - <sup>28</sup> L. A. Montoro, M. S. Leite, D. Biggemann, F. G. Peter-nella, K. J. Batemburg, G. Medeiros-Ribeiro, and A. J. Ramirez, *J. Phys. Chem C* **113**, 9018 (2009).
  - <sup>29</sup> Z. Zhong, W. Schwinger, F. Schäffler, G. Bauer, G. Vastola, F. Montalenti, and L. Miglio, *Phys. Rev. Lett.* **96**, 106102 (2007).